Internal frequency conversion extreme ultraviolet interferometer using mutual coherence properties of two high-order-harmonic sources

Sandrine Dobosz, H. Stabile, A. Tortora, P. Monot, F. Réau, M. Bougeard, H. Merdji, B. Carré, Ph. Martin, Denis Joyeux, et al.

AIP | Review of Scientific Instruments

Internal frequency conversion extreme ultraviolet interferometer using mutual coherence properties of two high-order-harmonic sources

S. Dobosz, H. Stabile, A. Tortora, P. Monot, F. Réau et al.

Citation: Rev. Sci. Instrum. **80**, 113102 (2009); doi: 10.1063/1.3257676
View online: http://dx.doi.org/10.1063/1.3257676
View Table of Contents: http://rsi.aip.org/resource/1/RSINAK/v80/i11
Published by the American Institute of Physics.

Internal frequency conversion extreme ultraviolet interferometer using mutual coherence properties of two high-order-harmonic sources

S. Dobosz,[1,a)] H. Stabile,[1] A. Tortora,[1] P. Monot,[1] F. Réau,[1] M. Bougeard,[1] H. Merdji,[1] B. Carré,[1] Ph. Martin,[1] D. Joyeux,[2] D. Phalippou,[2] F. Delmotte,[2] J. Gautier,[2] and R. Mercier[2]

[1]*CEA, IRAMIS, Service des Photons Atomes et Molécules, F-91191 Gif- sur-Yvette, France*
[2]*Laboratoire Charles Fabry de l'Institut d'Optique, CNRS et Université Paris Sud, Campus Polytechnique, RD 128, F-91127 Palaiseau cedex, France*

(Received 30 April 2009; accepted 11 October 2009; published online 3 November 2009)

We report on an innovative two-dimensional imaging extreme ultraviolet (XUV) interferometer operating at 32 nm based on the mutual coherence of two laser high order harmonics (HOH) sources, separately generated in gas. We give the first evidence that the two mutually coherent HOH sources can be produced in two independent spatially separated gas jets, allowing for probing centimeter-sized objects. A magnification factor of 10 leads to a micron resolution associated with a subpicosecond temporal resolution. Single shot interferograms with a fringe visibility better than 30% are routinely produced. As a test of the XUV interferometer, we measure a maximum electronic density of 3×10^{20} cm^{-3} 1.1 ns after the creation of a plasma on aluminum target. © *2009 American Institute of Physics.* [doi:10.1063/1.3257676]

I. INTRODUCTION

Interferometry in the visible domain has been extensively used to directly access the electronic density in laser-produced plasmas.[1] However, mostly due to refraction in high density gradients and reflection on overcritical regions, only electron densities typically lower than 10^{20} cm^{-3}–referred to as under critical–can be probed with visible light. Since the critical density scales as λ^{-2}, whereas refraction increases with λ, there is a strong interest for transferring plasma interferometry in the extreme ultraviolet (XUV) domain, where much higher densities can be probed. In addition, for probing fast-evolving plasmas such as plasma produced from picosecond or femtosecond laser pulses, the probe pulse duration must be even shorter to get snapshots of the density distribution at different times of the plasma evolution. In this respect, a transient inversion soft x-ray laser,[2,3] which delivers pulses of a few picosecond duration, makes possible picosecond x-ray laser interferometry of dense plasmas as demonstrated in Refs. 4–6. The high order harmonic (HOH) generation, either in gas or in plasma, offers another type of ultrashort–femtosecond down to attosecond–and flexible XUV source for imaging. In addition, it is naturally synchronized with the driving laser pulse, so that pump-probe type experiments with a (sub)femtosecond time resolution are greatly facilitated.

The real challenge with interferometry in the XUV domain arises from the difficulty to produce two mutually coherent beams, by either amplitude or wavefront division of one single XUV beam. In the first case, the manufacture of good quality XUV beam splitters is very demanding. In the second case, the XUV source should be highly spatially coherent. Furthermore, in both cases, the dividing optic edges can twist the fringe quality.[7] In general, the manipulation and transport of the XUV beam make it necessary to design dedicated optics–e.g., multilayer mirrors–which depart from grazing incidence geometry and which have thus a limited reflectivity. To save these advanced and expensive developments, the challenge is the design of an interferometer made of a minimum number of XUV optics. To that aim, a new type of interferometer has been introduced, without any beam division in the XUV.[8–10] In this new scheme, the two mutually coherent XUV sources were obtained by HOH generation, from two mutually coherent laser pulses focused in one and the same generating medium. Based on the highly coherent, laser-driven high harmonic generation, the frequency conversion from infrared (IR) to XUV takes place inside the interferometer, avoiding the use of XUV beam splitters. The two XUV sources, i.e., the laser pulses, could be either spatially separated[8] or temporally delayed.[9] Using HOH (11th order) of a Ti:sapphire (Ti:Sa) laser generated in gas, previous work performed by Descamps *et al.*[8] have reported the interferometric measurement of electron densities higher than 2×10^{20} cm^{-3}. These techniques have demonstrated the capability of unprecedented time resolution, of few 10 fs when probing with narrow band coherent XUV (200 fs demonstrated in Ref. 9). While the scheme with two pulsed gas jets, spatially separated, has the potential for two-dimensional (2D) imaging of plasma, it was not fully exploited in Ref. 8 where interferograms resulted from projection in the far field, i.e., did not really give an image of the plasma object. Note that the generation of the two mutually coherent sources in the same gas medium puts constraints on the interferometer geometry–the two arms are very close to each other–thus on the size of the object which can be probed.

a)Electronic mail: sandrine.dobosz-dufrenoy@cea.fr.

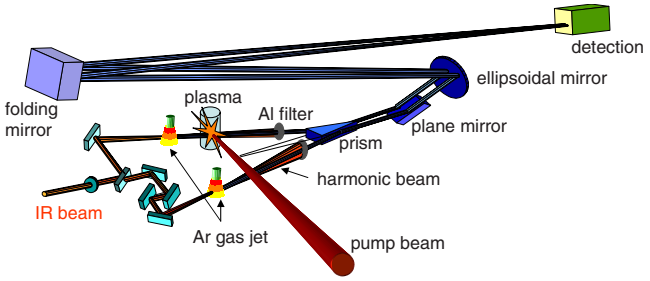

FIG. 1. (Color online) Experimental setup.

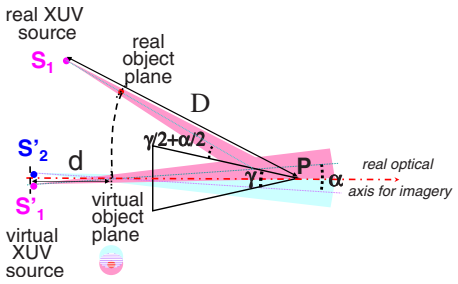

FIG. 2. (Color online) Principle of interference construction. The virtual sources, S_1' and S_2' from XUV point sources S_1 and S_2 (not reported here for clarity). Part of the reference arm is not reported here and angle α is larger than in reality for more readability. Virtual sources at a distance d from the object plane, act as Young's sources and generate interferences. A schematic view of the interference in the virtual object plane is reported, where the object and fringes are superimposed. Note that the virtual object/interferogram plane is centered onto the optical axis of the imaging device. Therefore, the real object is centered onto the image of the real optical axis into the reflecting face (angle $\frac{\gamma}{2}$), which is not the case of the real source (angle $\frac{\gamma}{2}+\frac{\alpha}{2}$).

In this paper, we present an innovative XUV interferometer free of XUV beam splitter specially based on HOH and designed for 2D imaging with a micron spatial resolution. In contrast with the previous schemes, the two mutually coherent XUV sources are now produced in two *independent spatially separated* gas jets, allowing for probing centimeter-sized objects. In this paper, we demonstrate for the first time that the two HOH sources generated in two different gas jets are mutually coherent, validating the basis concept of the instrument. We measure the coherence time of the HOH sources and show in our experimental conditions that the HOH signal level is sufficient to overcome the self-emission of a plasma generated by irradiation of solid aluminum target at maximum intensity of 3×10^{16} W/cm^2, 50 fs laser pulse duration. As an ultimate test, we measure a maximum electronic density of 3×10^{20} cm^{-3} 1.1 ns after irradiation at 3×10^{16} W/cm^{-2} of the target.

II. EXPERIMENTAL SETUP

The XUV interferometer, a schematic layout shown in Fig. 1, was set up on the LUCA laser facility (SLIC facility at CEA-Saclay, Ti:Sa laser at 800 nm, 50 mJ in 50 fs at 20 Hz). In the first stage, *the division and frequency conversion stage*, the IR beam is focused with a $f=1$ m lens and then split into two identical arms, i.e., two mutually coherent pulses, each containing 1–2 mJ. The two arms are then separately focused in two identical pulsed argon gas jet, respectively, under maximum intensity of 2×10^{14} W/cm^2, where HOH generation takes place. This results in two phase-locked HOH sources which are optimized, and XUV beams which form the two arms of the interferometer following the triangular geometry presented in Fig. 1. The dephasing object to be probed, for example a dense plasma, can be easily inserted with only weak constraints on its size, at distance $d=10$ cm from one of the XUV point sources, thus defining the object plane of the imaging optics. The high harmonic beam passing through the object is defined as the sample arm. The second one is called reference arm.

In a second stage, *the recombination stage*, the two arms are redirected by reflection on two faces of a prism (top angle $\gamma=12°$): the role of the redirecting prism is to produce two virtual XUV sources and one virtual object, in such a way that the beams from the virtual sources cross and interfere onto the virtual object, as illustrated in Fig. 2.

In the third last stage, *the imaging stage*, the virtual object and fringe pattern are imaged through an ellipsoidal mirror in the image plane where is the detector. Let us give some more details on the second *recombination stage* in Fig. 2. Each XUV point source (noted S_1 on Fig. 2) radiates a spherical wave, which is reflected onto the prism surface facing it, thus generating two virtual image sources. In the arrangement, the physical sources are placed symmetrically with respect to the reflecting prism bisector (which is also the imaging device optical axis). They are adjusted in such a way that the ray is incident onto the reflecting surface under $\frac{\gamma}{2}+\frac{\alpha}{2}$ (grazing), where α is a small angle (<1 mrad). The two virtual sources are therefore separated by distance αD, where D is the source to prism edge distance. Now, these virtual sources act as Young's sources, and generate interferences where the rays cross. The key principle of the instrument is to have the rays crossing and interfering in the virtual object plane, so that the object and the superimposed fringe pattern are imaged simultaneously in the detector plane. According to the geometry, the spacing of the fringe pattern is $\lambda\times$ (source-fringe)/(source separation), that is $\frac{\lambda d}{\alpha D}$. This virtual interference pattern with "embedded" object is then imaged into a real image with a magnification factor of 10. Accurate time overlap is adjusted with a (femtosecond) delay line on the reference arm. The recombination prism is a very delicate optic, with a surface quality better than $\frac{\lambda}{10}$ at 800 nm. This element is made of silica and has been manufactured by the Laboratoire Charles Fabry de l'Institut d'Optique. In the triangular geometry, the prism is used at incidence close to grazing, which means no specific multilayer coating to enhance the high reflectivity in the XUV domain. The counterpart of the grazing incidence is the large size of each side of the prism. One of the technical key points of this device is certainly the sharpness of the prism edge.

The imaging component is a high precision ellipsoidal mirror, which is diffraction limited at 32 nm on a 8×8 mm^2 pupil, at 6°, close to normal incidence. It has been made from a concave spherical surface of 1000 mm radius of curvature in which a cube of 30 mm side has been removed. An 8×8 mm^2 fraction of the surface has been shaped by

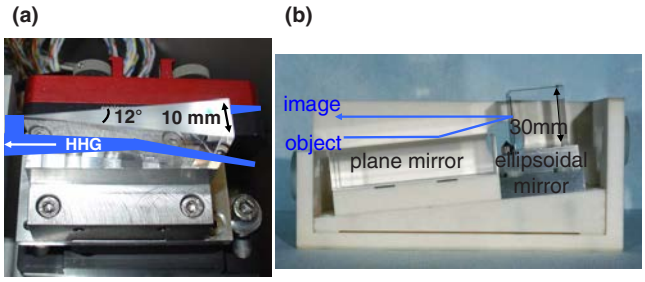

FIG. 3. (Color online) Photos of the silica prism (a) and of the "plane mirror–ellipsoidal mirror" ensemble (b) manufactured by the LCFIO-Orsay.

ionic erosion to obtain the ideal ellipsoidal shape profile, with an accuracy better than 0.5 nm rms on the surface profile.

Figure 3(a) shows a picture of the prism, 50 mm long and 10 mm base, with a sharp edge and a top angle of 12°. Figure 3(b) shows the imaging optical assembly composed of the plane mirror reflecting the two XUV beams toward the ellipsoidal mirror. The XUV beams are then reflected toward the folding mirror. The image axis is parallel to the object one with a vertical spacing of 10.4 mm. The focal length of the ellipsoidal mirror is $f=497.13$ mm. A final folding mirror is used to compact the whole instrument. The ellipsoidal imaging mirror is coated with B_4C/Si[11] multilayers in order to select the 25th HOH (H_{25}) at 32 nm, with a reflectivity of $23\pm3\%$ and high rejection ($R\leq5\%$) of adjacent harmonics H_{23} and H_{27}. The same coating has been put on the folding mirror and contributes to increase the rejection of H_{23} and H_{27}. The H_{25} harmonic gives the best compromise between high generation efficiency in Ar, good transmission through the aluminum filters ($\geq10\%$), good reflectivity of the multilayer coating, and measurable fringe spacing on the detector. The image detector consists of a pair of microchannel plates coupled to a phosphor screen, and has been placed at a distance close to 5.5 m of the ellipsoidal mirror to get a magnification of $G=10$.

The resolution of the optical device is given by the diffraction limit of the ellipsoidal mirror at 32 nm, corresponding to $R_{\text{ellipse}}\approx4$ μm in the object plane. As the final resolution R_{final} of the instrument depends on both the optical system and the detector, which spatial resolution is $R_{mcp}\approx30$ μm in the image plane, it can be evaluated using the following equation:

$$R_{\text{final}}=\sqrt{(G\cdot R_{\text{ellipse}})^2+R_{mcp}^2}\approx50\ \mu\text{m}.$$

The 50 μm spatial resolution in the image plane corresponds to 5 μm in the object plane. This resolution allows for imaging an object with a typical size of 50– 100 μm, with a sufficient sampling. In addition, the diameter of the detector is 22 mm which should allow for working with an effective field of ~2 mm in the object plane. This is well above the XUV beam size in our experimental conditions, as it will be seen in the following.

A typical single shot interferogram at 32 nm is reported in Figs. 4(a) and 4(b) (one-dimensional cut). The maximum visibility obtained reaches 30% for a fringe spacing of 12 μm in the object plane, corresponding to $\alpha\approx0.3$ mrad. The reproducibility of the interferograms is very good as the shot-to-shot visibility fluctuations are only of 15%. With this measurement, we experimentally demonstrate, for the first time, that the generation of two mutually coherent HOH sources is possible by focusing two phase-locked laser pulses into two different gas jets, thus pushing exploitation of the laser-driven coherence in high-harmonic generation beyond the results in Refs. 8–10 where the same jet was used. Though this result could be anticipated, it was far from granted that twin laser pulses could force phase-locking in highly nonlinear processes, driven in two mechanically identical but otherwise independent media. The interference field is 100×250 μm^2 in the object plane. The fringe spacing i can be tuned quite simply from 5 up to 13 μm by tilting the mirrors reflecting respectively IR beams toward gas jets, thus changing the angle α between the output XUV beams, respectively between 0.7 and 0.3 mrad. It can be noticed that the measured minimum fringe spacing of 5 μm is consistent with the ultimate theoretical spatial resolution of the interferometer, combination of the diffraction limit of the imaging optic, and the spatial resolution of the detector.

III. TEMPORAL COHERENCE MEASUREMENT

We have used this original interferometric instrument to measure the mutual temporal coherence of the two 25th har-

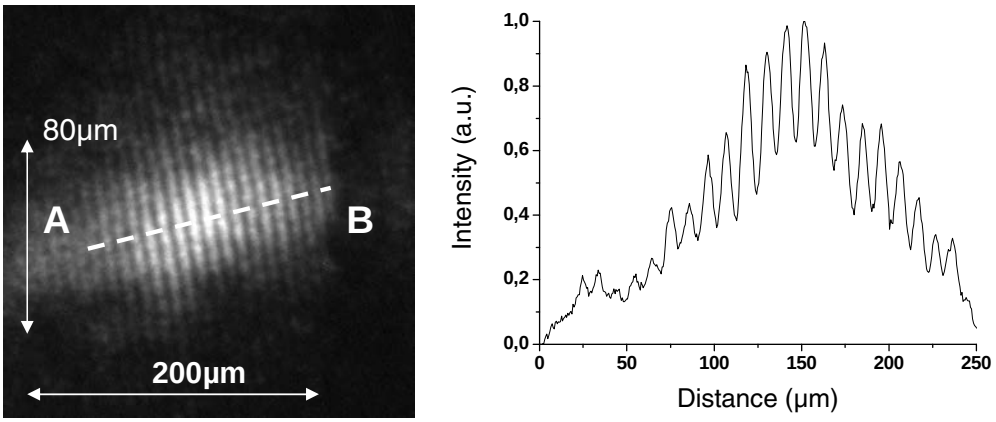

FIG. 4. Typical interferogram measured in the detector plane at 32 nm (left). The normalized intensity horizontal profile along the AB chord (right).

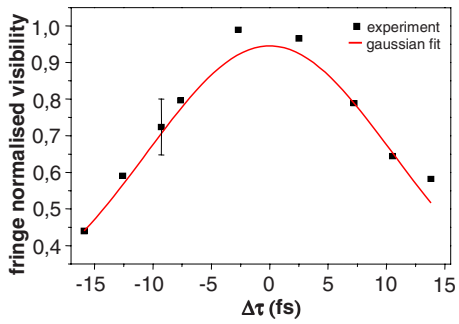

FIG. 5. (Color online) Normalized visibility of H_{25} fringes as a function of temporal delay $\Delta\tau$ between the two XUV arms of the interferometer.

monic sources. The coherence time τ_{coh} measures the correlation between the electromagnetic fields in the pulse temporal profile, and is directly related to the spectral width $\Delta\nu(\tau_{coh}\cdot\Delta\nu=0.44)$. A direct measurement of the coherence time can be obtained from measuring the fringe visibility in an amplitude division interferometer, that is as a function of the delay between the two arms. Using our interferometer, from the fringe patterns recorded over 30 fs time delay range between the reference and sample arms, we numerically extracted the normalized visibility over the whole interferogram.[12] The visibility function is plotted in Fig. 5. Now, the coherence time identifies to the half width at half maximum (HWHM) of the visibility function (also equal to the module of temporal coherence degree); we obtain $\tau_{coh}=12\pm1.2$ fs, that is $\frac{\Delta\lambda}{\lambda}\approx2\times10^{-3}$.

The τ_{coh} value is consistent with the pulse duration which can be estimated for HOH generated with 50 fs IR pulses, roughly equal to $\frac{50\ \text{fs}}{\sqrt{q_{eff}}}\sim20$ fs, where $q_{eff}\sim5$ is an effective order of nonlinearity for H_{25}.[13] This indicates that the longitudinal coherence is maintained almost throughout the full temporal profile.

The τ_{coh} value is also consistent with the previous studies performed on temporal coherence of HOH,[14,15] on Ti:Sa laser system delivering 100 fs IR pulses. The authors define a temporal coherence for inner and outer part of HOH far field spatial profile, the latter depending on the generation conditions and particularly on the position of the laser focus relative to the gas jet. In our case in Fig. 4, it can be noticed that the H_{25} spatial profile is centered, corresponding to on-axis phase matching when the IR laser is focused before the generating medium.[16] Finally, the coherence time determines the maximum *group delay*, i.e., of the order of 12 fs, which can be introduced by the dephasing object under study in our interferometer. Considering that the dephasing object is a plasma of length L, the maximum product (electron density)$\times$(plasma length) which can be probed is $\sim7.8\times10^{20}$ cm^{-2}. Besides the group delay boundary, the time resolution–that is the shortest characteristical time of evolution in a transient dephasing object, probed in a pump-probe type experiment–is given by the XUV pulse duration; in our conditions, it is of the order of 20 fs.

IV. XUV INTERFEROGRAM IN PRESENCE OF PLASMA

As the interferometer has been designed and set up to diagnose dense and transient plasma, one crucial point to address is the probe beam brilliance with respect to the plasma self-emission level. As a test case, a cylindrical aluminum target has been positioned in the object plane, i.e., in the interference field (fringe spacing set to 12 μm), and has been irradiated by an IR pump pulse of 50 fs duration, focused at a maximum intensity of 3×10^{16} W/cm^2. In Fig. 6, we compare (a) a typical reference harmonic interferogram at 32 nm obtained without plasma, and (b) the self-emission from the laser-produced plasma on the aluminum target. The target edge is materialized by a dotted vertical line.

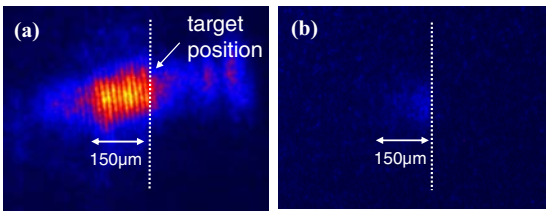

FIG. 6. (Color online) Reference interferogram without plasma (a). Self-emission from plasma created by irradiation of solid aluminum target at maximum intensity of 3×10^{16} W/cm^2(b).

In Fig. 7, we have extracted a horizontal profile from each image (in black the reference signal, in red the self-emission from Al plasma). As it can be seen clearly from both figures, the level of the spatially resolved self-emission is lower (by about a factor of 3) than the amplitude of the fringe modulation, whereas the spatially integrated self-emission is lower by one order of magnitude than the probe signal. In these typical experimental conditions for plasma studies, the plasma self-emission should thus not perturb the interferometric diagnose.

If we want to scale this to plasmas generated in relativistic regime,[17] it is important to consider the maximum noise level acceptable for analysis. First of all, we can mention that the spectral selectivity is ensured by the multilayer coating, B_4C/Si, which rejects 95% of adjacent harmonic and whose the ellipsoidal mirror and the folding mirror are covered with. Moreover, a geometrical selectivity contributes to the reduction in the noise level as the interferometer is imaging the object plane with a solid angle, extremely low (2.6×10^{-4} sr). Finally, recent experiments show that it's possible to generate up to 1 μJ of H_{25}.[18] Considering this en-

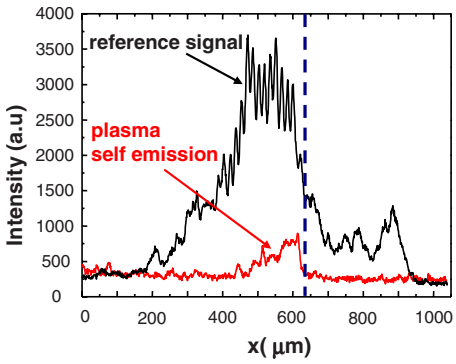

FIG. 7. (Color online) Profiles corresponding to reference signal from Fig. 6(a), without plasma, and to self-emission from plasma created by irradiation of solid aluminum target at maximum intensity of 3×10^{16} W/cm^2, from Fig. 6(b).

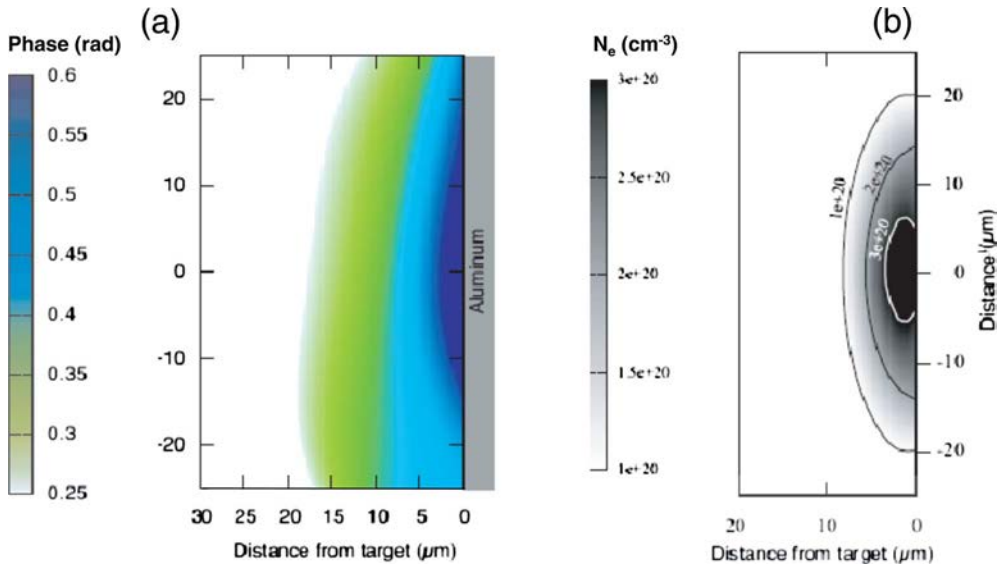

FIG. 8. (Color online) 2D phase map reconstructed for 1.1 ns delays between IR pump and XUV probe (a) and experimental electron density profile associated (b). The aluminum target is irradiated at 3×10^{16} W/cm^2, the laser is incident from the left.

ergy in the probe beam, the condition on plasma is to emit less than 2.6×10^{10} ph/mm^2 mrad^{2}1%BW at 32 nm to keep a signal-to-noise ratio lower than one, suitable for interferometer analysis.

As a proof of principle, we have tested the XUV interferometer on a plasma created by irradiation of solid aluminum target. The delay between the IR pump beam and XUV probe beam has been adjusted with a temporal delay line up to a few nanosecond after the creation of the plasma. The interferogram is very similar to the one presented in Fig. 6(a). A numerical treatment has been used as the fringe shift is not visible to the naked eye. A two-dimensional map of the phase shift $\delta\phi/2\pi$ between the two XUV beams (perturbed/reference) is reported on Fig. 8(a) for 1.1 ns time delay, directly extracted from fringe distortion, by performing a 2D-phase demodulation of the sinusoidal carrier by classical Fourier transform technique.[12] The fringe shift is related to the refractive index, n_{ref}, as $\delta\phi/2\pi=1/\lambda\int_0^L(1-n_{\mathrm{ref}})dl$, where L corresponds to the path length across the plasma, λ the probe wavelength, and the refractive index n_{ref} is given by $n_{\mathrm{ref}}=(1-n_e/n_c)^{1/2}$, with n_c the critical density associated to λ. Assuming a cylindrical symmetry of the plasma with respect to the pump beam propagation direction, we can extract the electronic density by using a standard Abel inversion,[19] this is shown in Fig. 8(b). Fringe shifts of 0.6λ measured close to the target surface corresponds to density of 3×10^{20} cm^{-3} at 1.1 ns. Considering that the minimum fringe shift is of the order of 1/10 fringe and that the probed plasma length is of the order of 50 μm, the minimum electronic density measurable is 2×10^{20} cm^{-3}. In our specific experimental conditions, the fringe shift is not clearly visible because of the reduced size of our plasma, combined to its low density.

V. CONCLUSION

In conclusion, we have presented a new scheme for a 2D-imaging interferometer based on amplitude division, working in the XUV range (here at 32 mm), specially designed to exploit the coherence properties of the HOH sources generated in gas. The original geometry of the interferometer avoids the difficulty of dividing the XUV beam, by dividing the IR driving beam and integrating the IR-to-XUV frequency conversion *inside* the interferometer. We validate the basic concept of the instrument by demonstrating the mutual coherence of the two XUV beams generated in two gas jets separated by a large distance (20 cm). Interferograms at 32 nm are routinely obtained at 20 Hz repetition rate using 50 fs IR beam with only 2–4 mJ energy. The interference field is close to 100×200 μm^2 in the object plane and the maximum contrast of the interferograms is 30%. Its ultimate spatial resolution is 5 μm, whereas the time resolution given by the XUV pulse duration is of a few 10 fs. The typical triangular geometry of the interferometer offers the possibility to accommodate large-sized objects under study. In a test case, we check that the brilliance of the HOH source makes it possible to study dense plasma on a solid target and we measure an electronic density of 3×10^{20} cm^{-3} at 1.1 ns, close to the target surface. Its compactness makes it a transportable diagnostic. Considering all its advantages, this innovative XUV interferometer could be well adapted for temporal diagnostics of high density plasma; it can be used also in a *reflection* geometry, to study the temporal evolution of crater formation on a solid target. More generally, the instrument can be adapted to any laser-driven XUV source, such as HOH generated in plasma,[20] of high brilliance ultrashort duration, and relatively compact. The XUV interferometry based on laser-driven mutual coherence should open perspectives in the context of, for example, the fast ignition scheme for energy production by inertial fusion.

This work was supported by the European Communities under the contract of Association between EURATOM and CEA within the framework of the European Fusion Programme, as well as by ACI "Photonique "2001 program.

[1] I. H. K. Muraoka, *Laser-Aided Diagnostics of Plasmas and Gases* (Bristol: Institute of Physics Pub, 2001).
[2] A. Klisnick, J. Kuba, D. Ros, R. Smith, G. Jamelot, C. Chenais-Popovics, R. Keenan, S. J. Topping, C. L. S. Lewis, F. Strati, G. J. Tallents, D. Neely, R. Clarke, J. Collier, A. G. MacPhee, F. Bortolotto, P. V. Nickles, and K. A. Janulewicz, Phys. Rev. A **65**, 033810 (2002).
[3] J. Filevich, J. J. Rocca, M. C. Marconi, R. F. Smith, J. Dunn, R. Keenan, J. R. Hunter, S. J. Moon, J. Nilsen, A. Ng, and V. N. Shlyaptsev, Appl. Opt. **43**, 3938 (2004).
[4] R. F. Smith, J. Dunn, J. Nilsen, V. N. Shlyaptsev, S. J. Moon, J. Filevich, J. J. Rocca, M. C. Marconi, J. R. Hunter, and T. W. Barbee, Phys. Rev. Lett. **89**, 065004 (2002).
[5] H. Tang, O. Guilbaud, G. Jamelot, D. Ros, A. Klisnick, D. Joyeux, D. Phalippou, M. Kado, M. Nishikino, M. Kishimoto, K. Sukegawa, M. Ishino, K. Nagashima, and H. Daido, Appl. Phys. B: Lasers Opt. **78**, 975 (2004).
[6] J. Filevich, J. J. Rocca, M. C. Marconi, S. J. Moon, J. Nilsen, J. H. Scofield, J. Dunn, R. F. Smith, R. Keenan, J. R. Hunter, and V. N. Shlyaptsev, Phys. Rev. Lett. **94**, 035005 (2005).
[7] L. Le Déroff, P. Salières, B. Carré, D. Joyeux, and D. Phalippou, Phys. Rev. A **61**, 043802 (2000).
[8] D. Descamps, C. Lyngå, J. Norin, A. L'Huillier, C. G. Wahlstrom, J. F. Hergott, H. Merdji, P. Salières, M. Bellini, and T. W. Hänsch, Opt. Lett. **25**, 135 (2000).
[9] P. Salières, P. Antoine, A. De Bohan, and M. Lewenstein, Phys. Rev. Lett. **83**, 5483 (1999).
[10] R. Zerne, C. Altucci, M. Bellini, M. B. Gaarde, T. W. Hansch, A. L'Huillier, C. Lyngå, and C. G. Wahlstrom, Phys. Rev. Lett. **79**, 1006 (1997).
[11] F. Delmotte, J. Gautier, M. F. Ravet, F. Bridou, and A. Jerome, J. Phys. IV **127**, 69 (2005).
[12] O. Guilbaud, H. Tang, D. Joyeux, G. Jamelot, A. Klisnick, D. Ros, D. Phalippou, K. Cassou, M. Kado, M. Nishikino, K. Sukegawa, M. Kishimoto, M. Ishino, K. Nagashima, and H. Daido, J. Phys. IV **127**, 63 (2005).
[13] T. E. Glover, R. W. Schoenlein, A. H. Chin, and C. V. Shank, Phys. Rev. Lett. **76**, 2468 (1996).
[14] M. Bellini, C. Lyngå, A. Tozzi, M. B. Gaarde, T. W. Hansch, A. L'Huillier, and C. G. Wahlstrom, Phys. Rev. Lett. **81**, 297 (1998).
[15] C. Lyngå, M. B. Gaarde, C. Delfin, M. Bellini, T. W. Hansch, A. L'Huillier, and C. G. Wahlstrom, Phys. Rev. A **60**, 4823 (1999).
[16] H. Merdji, M. Kovacev, W. Boutu, P. Salières, F. Vernay, and B. Carré, Phys. Rev. A **74**, 043804 (2006).
[17] R. A. Snavely, B. Zhang, K. Akli, Z. Chen, R. R. Freeman, P. Gu, S. P. Hatchett, D. Hey, J. Hill, M. H. Key, Y. Izawa, J. King, Y. Kitagawa, R. Kodama, A. B. Langdon, B. F. Lasinski, A. Lei, A. J. MacKinnon, P. Patel, R. Stephens, M. Tampo, K. A. Tanaka, R. Town, Y. Toyama, T. Tsutsumi, S. C. Wilks, T. Yabuuchi, and J. Zheng, Phys. Plasmas **14**, 092703 (2007).
[18] A. Ravasio, D. Gauthier, F. R. N. C. Maia, M. Billon, J.-P. Caumes, D. Garzella, M. Géléoc, O. Gobert, J.-F. Hergott, A.-M. Pena, H. Perez, B. Carré, E. Bourhis, J. Gierak, A. Madouri, D. Mailly, B. Schiedt, M. Fajardo, J. Gautier, P. Zeitoun, P. H. Bucksbaum, J. Hajdu, and H. Merdji, Phys. Rev. Lett. **103**, 028104 (2009).
[19] I. H. Hutchinson, *Principles of Plasma Diagnostics* (Cambridge University Press, Cambridge, 2005), p. 458.
[20] C. Thaury, F. Quéré, J.-P. Geindre, A. Levy, T. Ceccotti, P. Monot, M. Bougeard, F. Réau, P. D'Oliveira, P. Audebert, R. Marjoribanks, and Ph. Martin, Nat. Phys. **3**, 424 (2007).